Electronic supplementary information (ESI):

Hierarchically nanoporous nickel-based actuators with giant reversible strain and ultrahigh work density

Qingguo Bai,[a] Yan Wang,[b] Jie Zhang,[a] Yi Ding,[c] Zhangquan Peng,[d] Zhonghua Zhang[a],*

[a]*Key Laboratory for Liquid–Solid Structural Evolution and Processing of Materials (Ministry of Education), School of Materials Science and Engineering, Shandong University, 17923 Jingshi Road, Jinan 250061, P.R. China.* Email: zh_zhang@sdu.edu.cn.

[b]*School of Materials Science and Engineering, University of Jinan, 336 West Road of Nan Xinzhuang, Jinan 250022, P.R. China.*

[c]*School of Materials Science and Engineering, Tianjin University of Technology, 391 Binshui Xidao, Xiqing District, Tianjin 300384, P.R. China.*

[d]*State Key Laboratory of Electroanalytical Chemistry, Changchun Institute of Applied Chemistry, Chinese Academy of Sciences, Renmin Road 5625, Changchun 130022, P.R. China*

Notes

1. **Sample preparation**

2. **Microstructural characterization**

3. **Actuation measurement**

4. **Calculation of NiO layers on the surface of np-Ni**

5. **Calculation of specific capacitance**

6. **Figures (Figure S1-Figure S20) and Tables (Table S1-Table S3)**

7. **References**

Other supplementary materials for this manuscript include the following:

Movie S1

Flash S1

1. Sample preparation

Al-Ni precursor alloys with nominal compositions of 20, 25 and 31.5 at. % Ni were prepared from pure Al (99.99 wt. %) and Ni (99.99 wt. %) by high-frequency induction heating in a quartz crucible. The Al-20, 25 and 31.5 at. % Ni alloys were denoted as $Al_{80}Ni_{20}$, $Al_{75}Ni_{25}$ and $Al_{68.5}Ni_{31.5}$ for simplicity, respectively. The melt was cast into ingots in an iron chill mold. Small parts of the ingots were remelted in a quartz tube, and Al-Ni alloy rods with different diameters were then obtained by blow-casting in a copper mold. Before dealloying, the Al-Ni rods were annealed at 300 °C for 10 h to remove the residual stress. Cylinder samples with different diameters and lengths were cut from the Al-Ni rods. Nanoporous nickel (np-Ni) samples were prepared by dealloying the Al-Ni rods in a 6 M KOH aqueous solution which was prepared from KOH (analytical reagent, AR) and ultra-purified water (18.2 MΩ.cm). The dealloying was performed firstly at room temperature and a large amount of bubbles emerged. The dealloying was then carried out at 90 ± 5 °C to further remove the residual Al until no obvious bubbles appeared. The samples underwent a slight volume contraction during dealloying, which is similar to the volume change of nanoporous gold (NPG) during dealloying[34]. After dealloying, the np-Ni samples were rinsed using ultra-purified water to remove the residual ions (K^+, OH^-, etc.). Thus, the np-Ni rods with different diameters and lengths were obtained (Figure S3). It should be noted that the np-Ni samples which were obtained from the $Al_{80}Ni_{20}$ precursor, were too 'soft' to be well handled and were not suitable for the actuation measurements. In addition, the np-Ni samples in this work referred to those

which were prepared by the dealloying of the $Al_{75}Ni_{25}$ precursor unless otherwise stated.

The relative density (φ) of our np-Ni samples could be calculated through the equation $\varphi = \rho_{np} / \rho_s$[31], where ρ_{np} is the density of np-Ni and ρ_s is the density of bulk Ni. The ρ_{np} could be obtained from the mass of np-Ni divided by its volume. The relative density of np-Ni was determined to be $\varphi \approx 0.3$. Thus the porosity of our np-Ni samples was ~ 70%.

2. Microstructural characterization

The macrographs of the Al-Ni precursors and np-Ni samples were taken using a digital camera. The section-view microstructure of the Al-Ni precursor and the np-Ni samples was observed using a scanning electron microscope (SEM, LEO 1530 VP). The nanoporous structure of np-Ni was characterized by a transmission electron microscope (TEM, FEI Tecnai G2). The selected-area electron diffraction (SAED) was further documented to identify the phase constitution of np-Ni. The X-ray diffraction (XRD) results confirmed that the np-Ni samples are composed of the single face centered cubic (f.c.c.) Ni phase. In addition, according to the literature data[35], a Brunauer–Emmett–Teller (BET) specific surface area of ~60 m^2/g was assumed for the present np-Ni samples.

3. Actuation measurement

In order to measure the electrochemical actuation properties of our np-Ni samples, a three-electrode system was constructed (inset of Figure 2a). The np-Ni rod was used as the working electrode (WE). A Pt plate and saturated calomel electrode (SCE) were used as the counter electrode (CE) and reference electrode (RE), respectively. The electrochemical data (cyclic voltammetry (CV), square wave potential sweeping, etc.) were collected using a potentiostat (CHI 660E). The np-Ni samples were mounted between a fixed stand and a pushrod (inset of Figure 2a). The electrochemically induced expansion/contraction strain of the np-Ni samples was recorded using a displacement sensor through the pushrod. Here, the influence (for example, the compression) of the pushrod on the measurement has been calibrated or compensated by the supplier. The actuation properties of the np-Ni samples were measured in different alkaline electrolytes (NaOH or KOH) with different concentrations (2 or 5 M) which were prepared from analytical reagents and ultra-purified water. The results demonstrated that similar actuation data were obtained in different electrolytes (2 M NaOH, 5 M NaOH or 5 M KOH) under identical testing conditions (see Figure S20). Thus the 5 M NaOH aqueous solution was used as the electrolyte in the other actuation experiments in this work.

In addition, in order to examine the response of our np-Ni actuators to two-position input signals, we constructed a model actuator with two positions (electrodes). The np-Ni sample and Ni-foam supported carbon were used as the positive and negative electrodes, respectively (Figure 5a). The Ni-foam supported carbon electrode

was prepared as follows. Firstly, the activated carbon (TF-B520) was mixed with conductive carbon black (TIMICAL SuperC45) and polyvinlidene fluoride (PVDF), and their mass ratio is 8:1:1. Then, N-methyl pyrrolidone was added into the mixture as a solvent. The mixture was stirred to make a slurry and the slurry was homogeneously coated onto a nickel foam (1cm×1cm). Finally, the carbon-coated Ni foam was dried in vacuum at 120 ^{o}C for 5 h to remove the solvent, and thus used as the negative electrode. The cyclic voltammetry, square wave potential sweeping and charging-discharging data were recorded by the CHI 660E potentiostat. At the same time, the responding reversible strain of the model actuator was measured by the displacement sensor (Figure 5a).

4. **Calculation of NiO layers on the surface of np-Ni**

Here, the atomic layers of Ni oxide could be evaluated as follows. Assuming 2 electrons per oxidized Ni atom (Ni→NiO), defining one equivalent monolayer as the density of Ni atoms on a Ni(111) surface (the (111) is taken as an example), 18.6 nm^{-2}, taking the sample mass of M, the specific surface area ($\alpha_M = 60$ m^2/g) and the net charge ($Q=65$ C) involved in the oxidation process of Ni which could be calculated from the CV curves, with the electron charge e, the atomic layers N could be calculated by the formula: $N=Q/(18.6eM\alpha_M)$. Thus we can get the 1-2 atomic layers for NiO.

5. Calculation of specific capacitance

Specific capacitance (C, F/g) values of the np-Ni samples were determined from the CV curves according to the equation[36],

$$C = \frac{1}{mv\Delta V} \int I(V)dV$$

where $I(V)$ is the oxidation/reduction current, m is the mass of the active electrode materials (here, np-Ni), v is the potential scan rate and ΔV is the potential range of one CV segment.

6. Figures and Tables
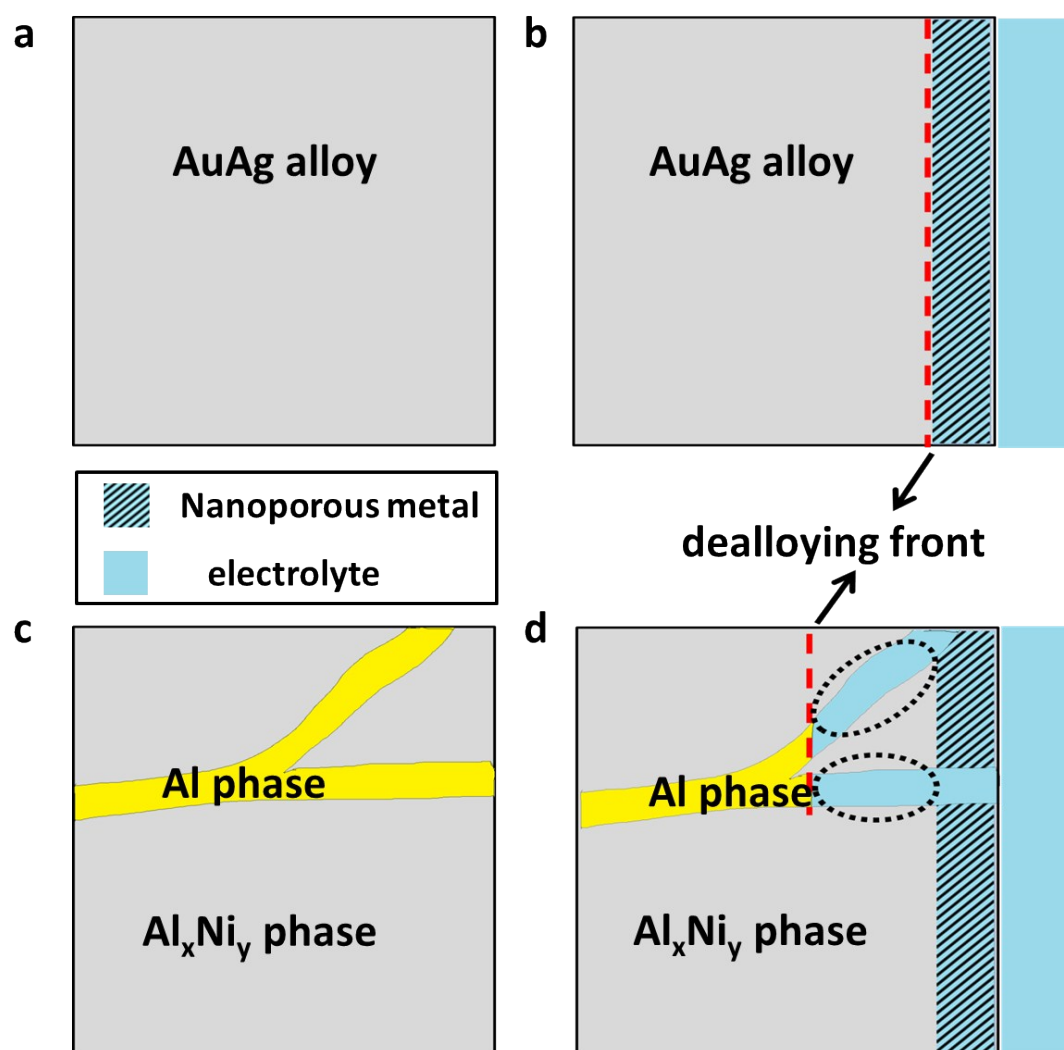
Figure S1 | Schematic illustration of dealloying in two kinds of alloy systems. (a,b) Homogeneous solid alloys like AuAg. (**c,d**) Hybrid-phase (two-phase or multi-phase) precursor alloys like Al-Ni composed of one less noble phase (which can be completely etched away leaving large-sized channels, for example, Al phase) and at least one more noble phase (which can be dealloyed to form a nanoporous structure, Al_xNi_y phase). (**a,c**) Before dealloying and (**b,d**) during dealloying. As to AuAg, Ag will be selectively dissolved and the remaining Au adatoms diffuse and re-organize into a nanoporous structure when dealloying in a solution like concentrated HNO_3[25].

The dealloying front is located between the un-dealloyed part and the nanoporous zone, as marked by a dashed line in Figure S1b. The electrolyte can go to the dealloying front through the nano-sized channels but will be greatly hindered due to their small sizes. With the moving of the dealloying front towards the inner part of the sample, the dealloying rate will slow down owing to the nano-sized channels and limited mass transfer. Therefore, **it is quite difficult to fabricate bulk nanoporous metals or alloys through dealloying the homogeneous solid solution alloys like AuAg**. For the Al-Ni alloys composed of Al and Al_xNi_y phases, the Al phase can be completely etched away in an alkaline solution like NaOH, leaving large channels (several to tens of microns, see Figure S1d). At the same time, the Al_xNi_y phases can be dealloyed to form the nanoporous structure. The electrolyte can quickly penetrate into the inner part of the sample through these large channels, and the dealloying front can move forward much faster than the scenario of the homogeneous solid alloy like AuAg. Moreover, the etching of the Al phase makes the dealloying occur in localized zones around the large channels (as highlighted by dotted ellipses in Figure S1d). This phenomenon can be designated as 'localized dealloying'. Even for bulk samples, the dealloying can rapidly extend into the inner of the samples through this 'localized dealloying' mode. Thus, bulk hierarchically nanoporous samples can be fabricated by this unique dealloying strategy.
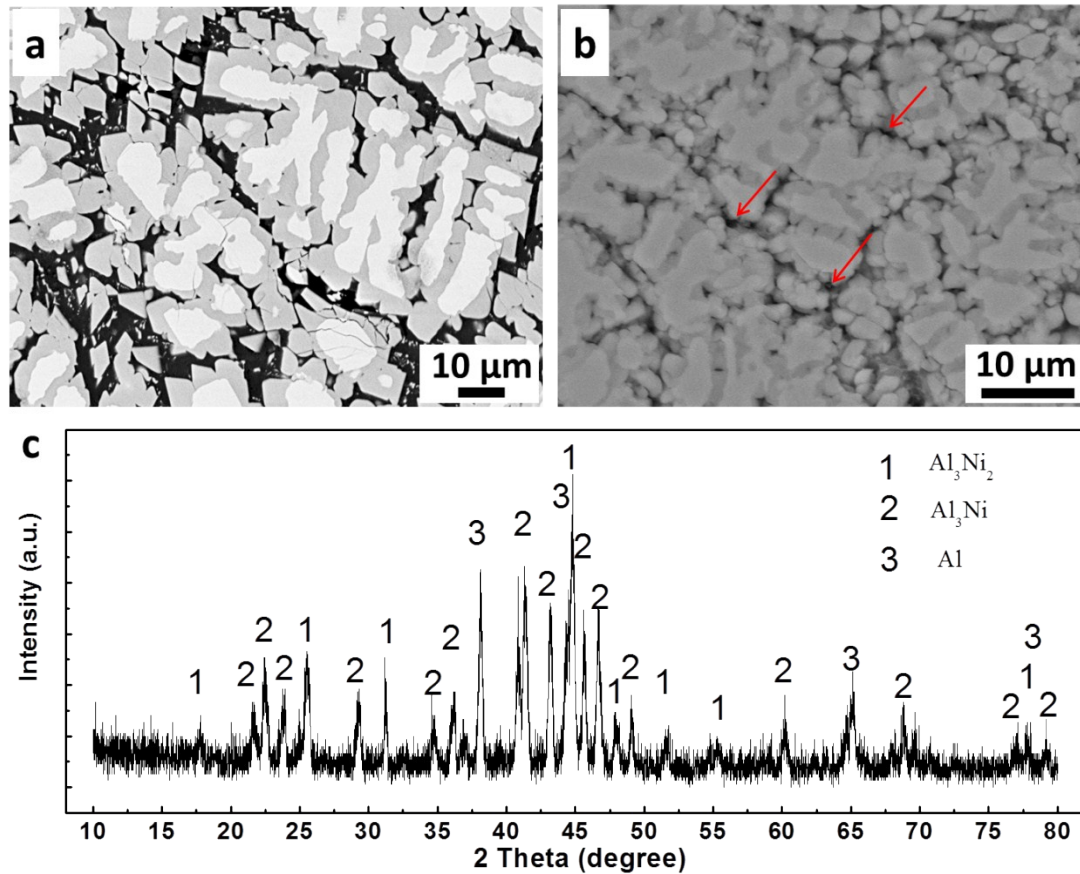
Figure S2 | (a) Back-scattered electron (BSE) image of the section of a $Al_{75}Ni_{25}$ alloy rod. Three areas can be identified. The energy dispersive X-ray (EDX) results show that the bright grey areas are Al_3Ni_2 phase, the grey areas are Al_3Ni phase, and the dark areas are α-Al phase. Most of Al_3Ni_2 is surrounded by Al_3Ni, and the α-Al phase interpenetrates with the Al_xNi_y (Al_3Ni_2 and Al_3Ni) phases. Moreover, the Al_3Ni_2 and Al_3Ni phases form a dendirte morphology. **(b)** Section-view SEM image of the $Al_{75}Ni_{25}$ rod after 1 min of immersion in a 0.5 wt.% HF solution. The rod was slightly corroded during this immersion. The α-Al phase was selectively corroded away, leaving large-sized channels among the un-corroded Al_xNi_y dendrites (as highlighted by red arrows in Figure S2b). The solution could easily go into the inner of the Al-Ni rod through these bicontinous interpenetrating channels during dealloying. **(c)** XRD pattern of the bulk $Al_{75}Ni_{25}$ alloy rod. Three phases (α-Al, Al_3Ni_2 and Al_3Ni) can be

identified, which is consistent with the BSE result in (a).

The above results demonstrate that the Al-Ni alloys (for example, $Al_{75}Ni_{25}$) can meet the alloy design (more than two phases with different corrosion activities) of 'localized dealloying' for bulk samples. Actually, we have obtained bulk nanoporous Ni rods with different diameters and lengths through dealloying of Al-Ni rods in alkaline solutions.
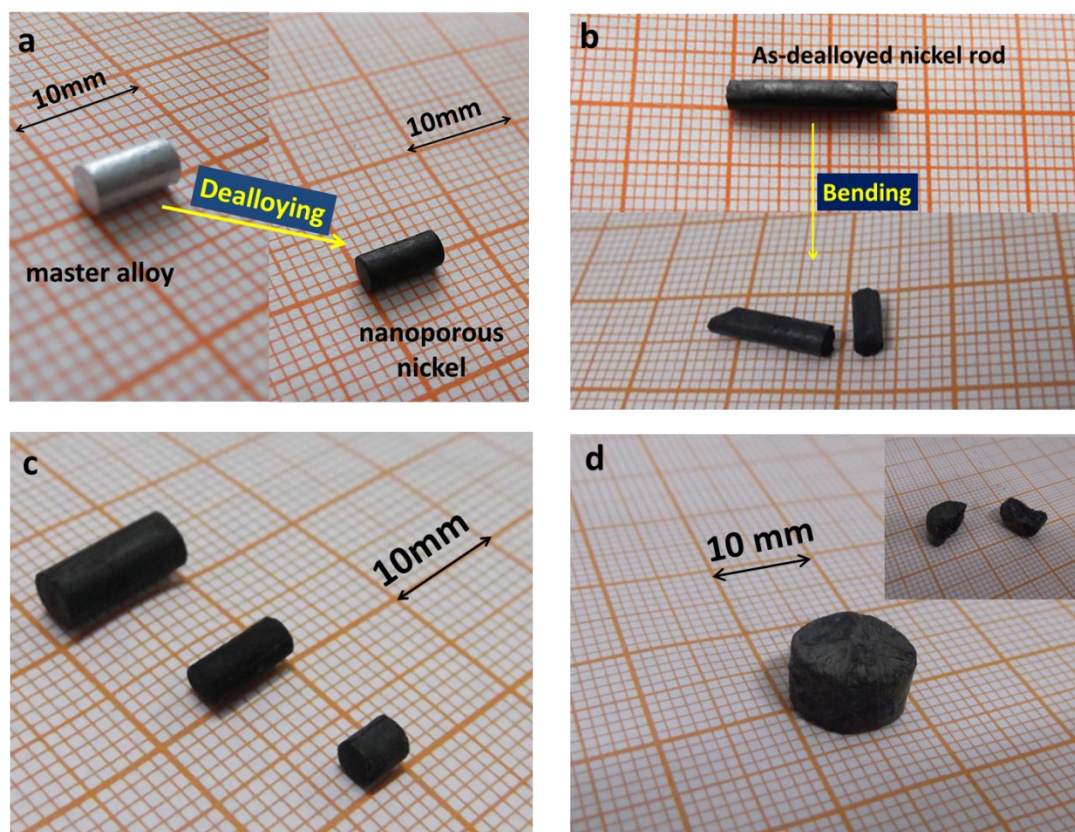
Figure S3 | Macrographs of the Al$_{75}$Ni$_{25}$ precursor and the np-Ni samples prepared by the dealloying in 6 M KOH solution. (**a**) The master (precursor) alloy rod before dealloying (left) and np-Ni sample after dealloying (right). (**b**) Macrographs of the np-Ni rod before and after the bending process. (**c**) Macrograph of the np-Ni rods with different sizes (different lengths and diameters). (**d**) Macrograph of the np-Ni rod with the diameter of 10 mm. The inset shows the two parts of the broken np-Ni rod, indicating that the porous structure goes through the whole section of the sample. It is clear that the size (length or diameter) of the np-Ni rods can reach up to centimeters, which are crucial for their practical applications in actuators. Moroever, the np-Ni samples with different shapes (like cubes, plates, etc.) can also be fabircated through control over the shape of the precursor alloys.
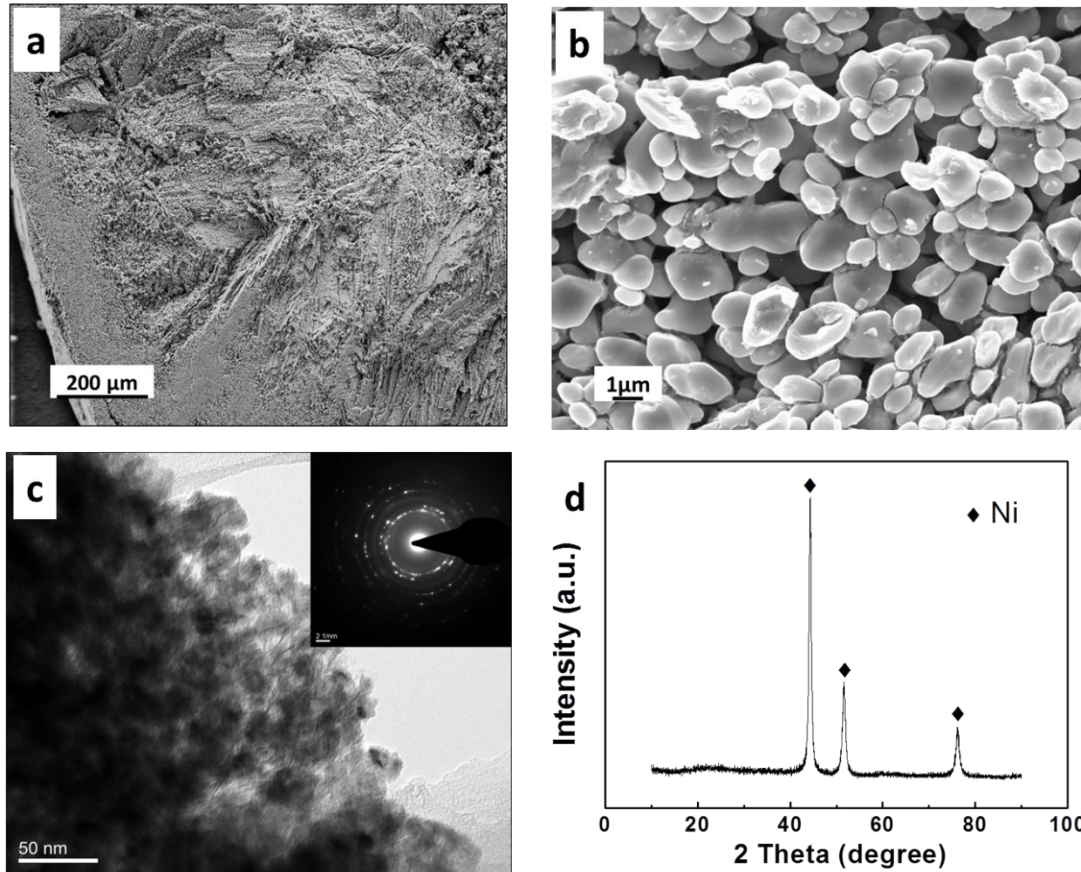
Figure S4 | Microstructure of the np-Ni samples prepared by dealloying of the Al$_{75}$Ni$_{25}$ alloy in the 6 M KOH solution. (**a**) Section-view SEM image of the np-Ni rod and (**b**) an enlarged SEM image at higher magnification. (**c**) TEM image showing the nanoporous structure of the np-Ni samples and (inset) corresponding SAED pattern. (**d**) Typical XRD pattern of the np-Ni samples. Both the XRD and electron diffraction results confirm that the np-Ni samples are composed of the single face centered cubic (f.c.c.) Ni phase.
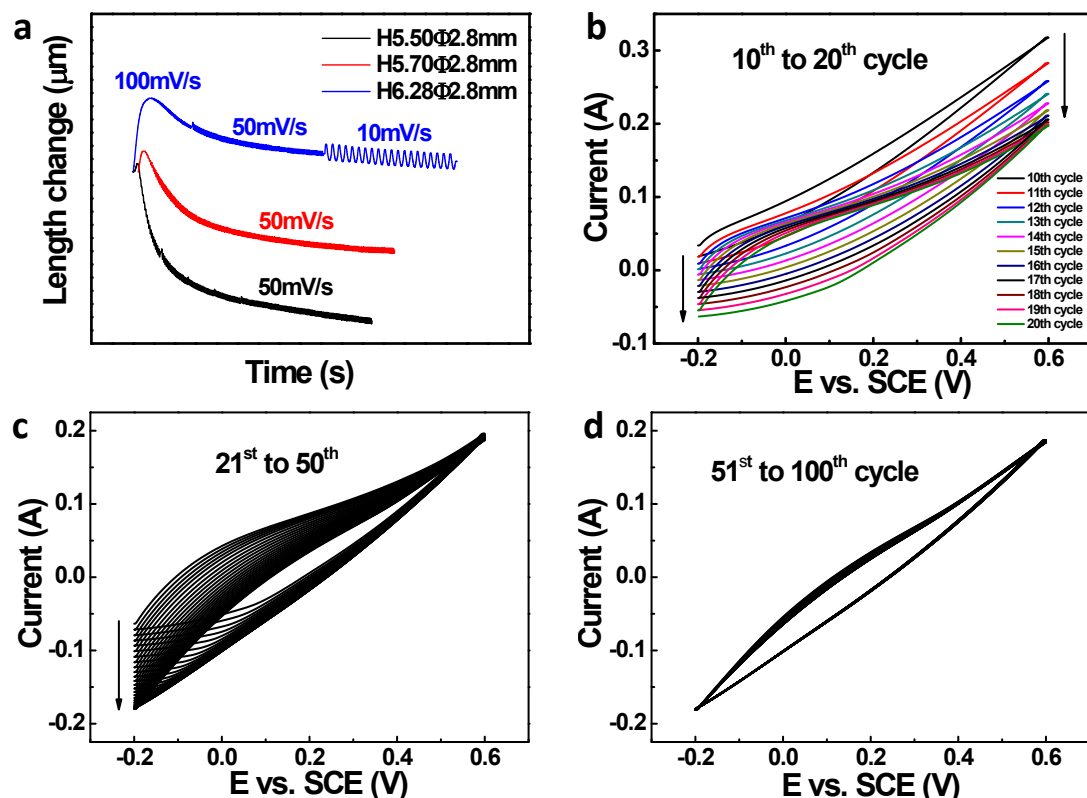
Figure S5 | (**a**) Length change of the np-Ni samples during the initial CV cycles in the 5 M NaOH solution. Both reversible expansion/contraction strain and irreversible contraction could be observed. The irreversible contraction gradually decreases with increasing CV cycles, and the samples tend to be stable. The sizes of np-Ni are marked in the top-right corner of this panel. The scan rates of CV are also labeled near the strain curves. (**b-d**) Typical evolution of the CV curves with increasing cycles. The CV profiles tend to be stable with the increase of cycles, and almost overlap after the 50th cycle.

Based upon the dealloying mechanism,[37] the active element (here, Al) is always residual in the as-dealloyed samples. When being subjected to electrochemical treatment, the residual Al could be further removed.[38] At the same time, Ni would be oxidized in the alkaline media in the potential range (-0.2~0.6 V vs. SCE). Before the

20th cycle, the irreversible oxidation/reduction reactions occur in the CV processes. And the oxidation currents are much higher than the reduction currents, indicating the formation of nickel oxide on the ligament surface of np-Ni and also the active dissolution of residual Al atoms in the np-Ni sample. [38] Moreover, the current value at the end of potential window decreases greatly with increasing CV cycles at the beginning, suggesting the gradual saturation of the O-adsorption sites. In the last 50 cycles, the CV profiles tend to be stable and are associated with the reversible OH$^-$ adsorption/desorption of the oxide-covered np-Ni.
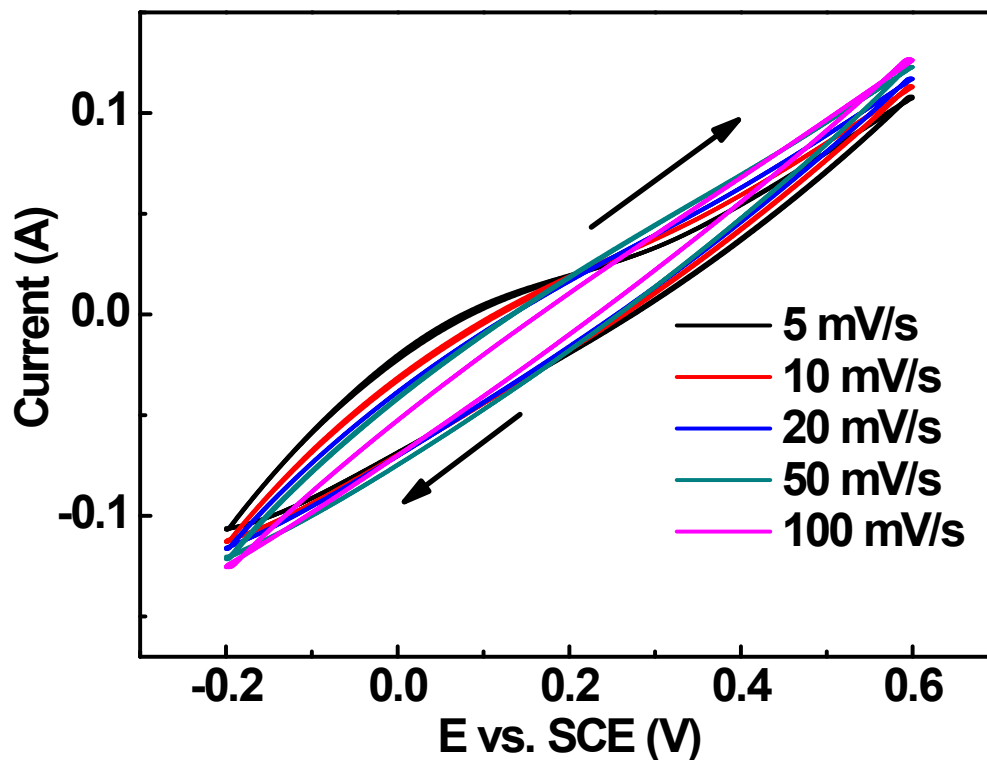
Figure S6 | CV curves of the np-Ni sample in the 5 M NaOH solution at different scan rates. Compared with the CV curves recorded at the lower scan rates (such as 0.1 and 0.2 mV/s, Figure 2b), the OH adsorption/desorption peaks could not be distinguished. This may be associated with the bulk sample size, the higher scan rate and the limitations by the diffusion kinetics in the nanopore space[11].
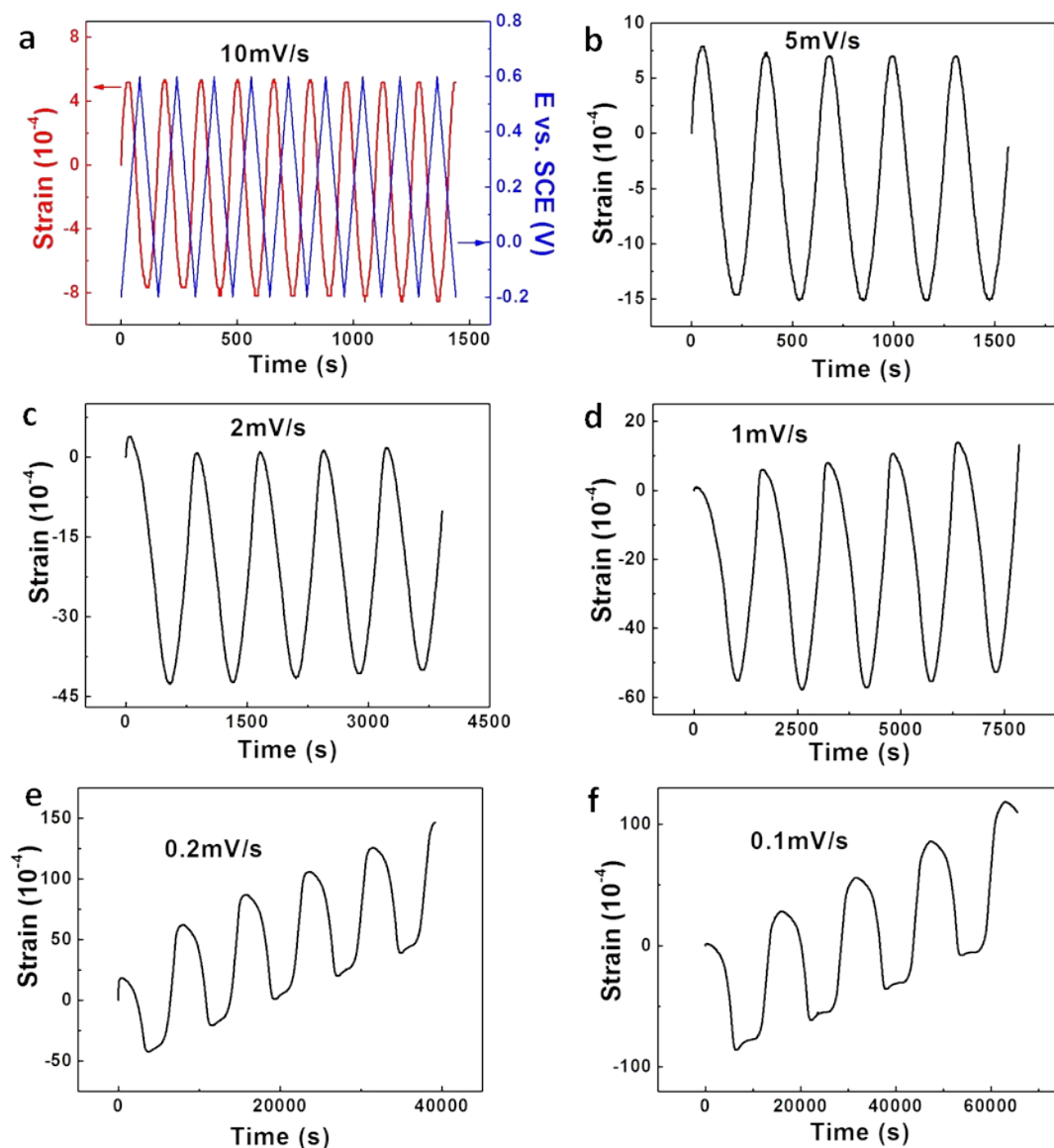
Figure S7 | (a) Typical reversible strain of the np-Ni sample versus time, together with the potential variation during nine successive CV cycles at the scan rate of 10 mV/s. **(b-f)** Reversible strain of the np-Ni sample versus time during successive CV cycles between - 0.2~0.6 V vs. SCE at different potential scan rates (marked on each panel). At the scan rate of above 1 mV/s, the reversible strain shows excellent stability with increasing CV cycles (a-d). However, a noticeable irreversible strain could be observed on the strain-time curves at the slower scan rates of 0.1 and 0.2 mV/s (e-f).
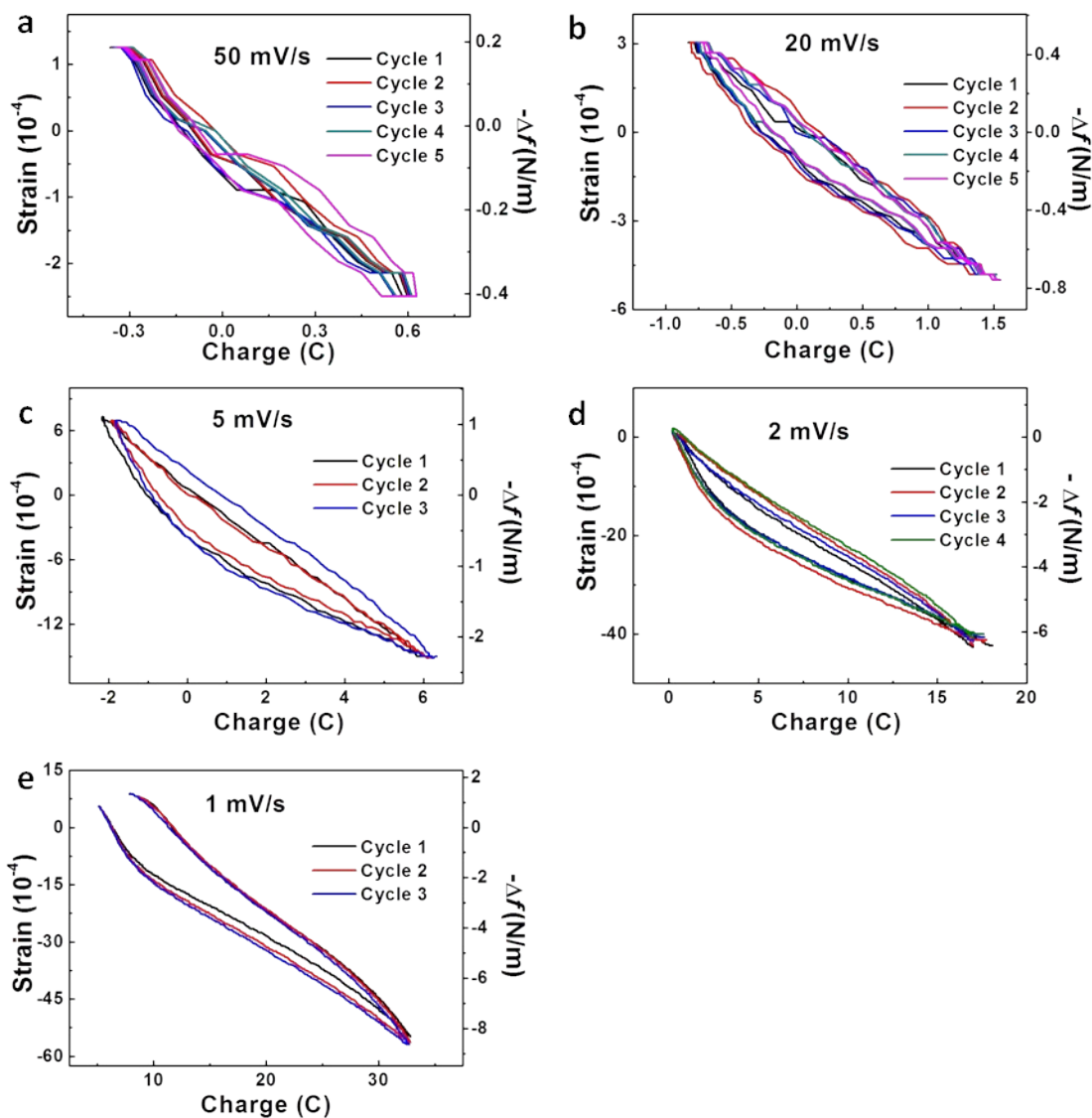
Figure S8 | The plots of the reversible strain (left coordinate) of the np-Ni samples versus the transferred charge during the CV processes at different scan rates (marked on each panel). An obvious negative correlation could be observed between the reversible strain and the transferred charge, which indicates the nature of the oxide-covered surface of the np-Ni samples[11,14-16]. The variation of charge-induced surface stress ($-\Delta f$) is also presented as the right coordinate. In addition, at least three successive CV scans were carried out at each scan rate, and the superposition of the strain-charge curves indicates excellent reproducibility.
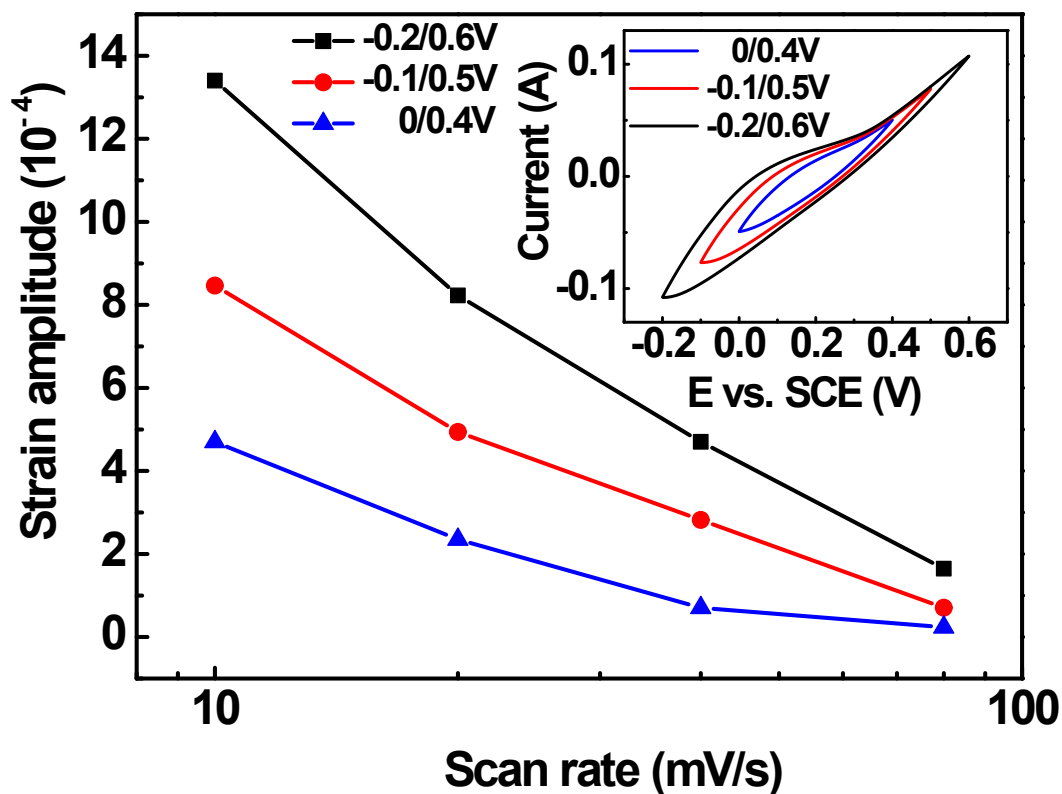
Figure S9 | The reversible strain amplitude of the np-Ni sample versus the scan rate during the CV processes with different potential windows (as marked in the panel). Both the scan rate and the potential window have a significant influence upon the reversible strain amplitude of the np-Ni samples. On one hand, we can modulate the reversible strain amplitude through changing the applied potential window. On the other hand, the strain amplitude could also be tuned by varying the potential scan rate, when the sample was measured in different scan windows. (Inset) Typical CV curves of the np-Ni samples in different potential windows at the scan rate of 10 mV/s.
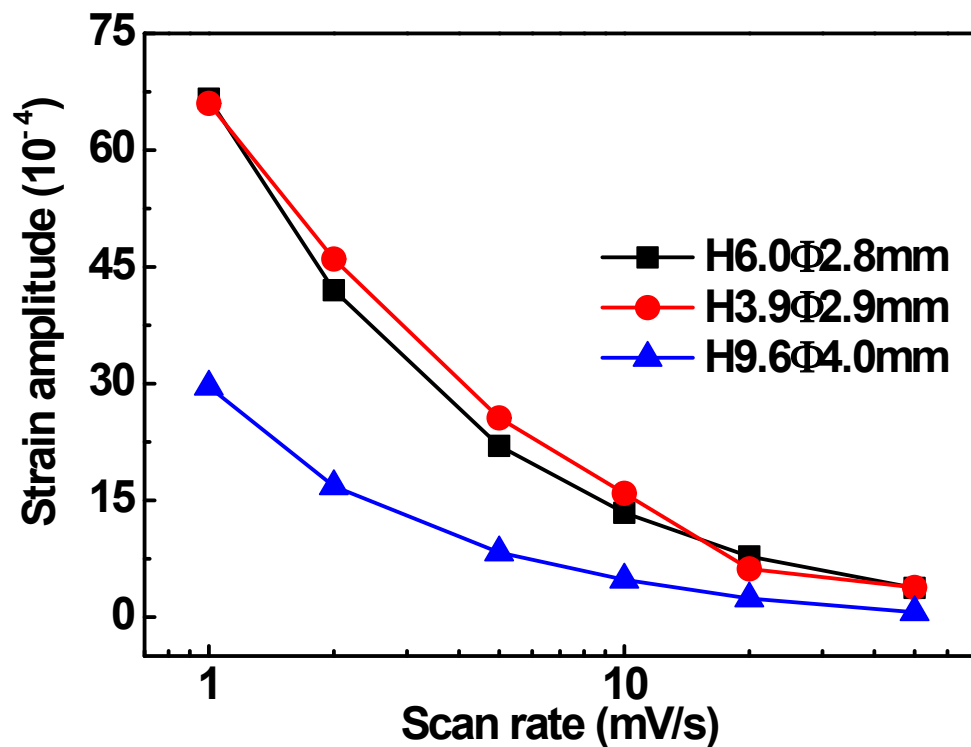
Figure S10 | The reversible strain amplitude of the np-Ni samples with different sizes (diameters/lengths, marked in the panel; 'H' and 'Φ' denote the length (or height) and diameter of the np-Ni samples respectively.) versus the scan rate during the CV processes with the potential window of - 0.2~0.6 V vs. SCE in the 5 M NaOH aqueous solution. In this work, the bulk np-Ni rods with different sizes (Figure S3c) were prepared by the dealloying of the $Al_{75}Ni_{25}$ precursor in the 6 M KOH solution. All the np-Ni rods show good electrochemical actuation behaviors. For practical applications, the np-Ni actuators with different bulk sizes could meet diverse requirements.
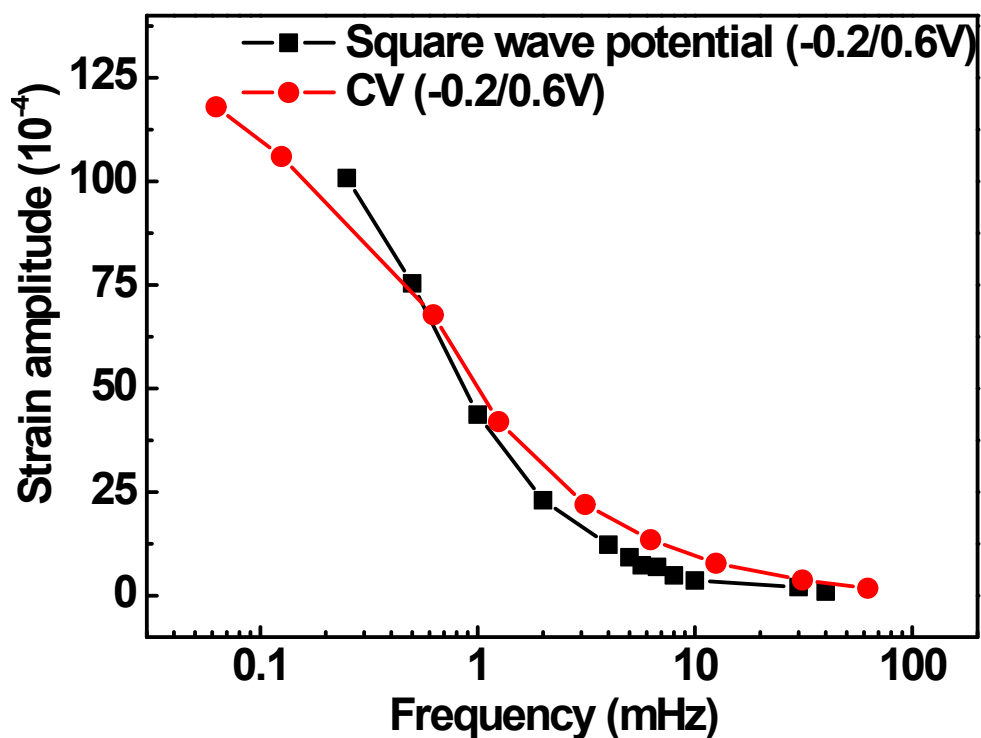
Figure S11 | The reversible strain amplitude of the np-Ni samples versus the applied frequency. Red solid circles: the results were calculated from the plot of the reversible strain versus the scan rate (potential window: - 0.2~0.6 V vs. SCE, Figure 2g); black solid squares: the frequency was determined from the square wave potential experiments (potential window: - 0.2~0.6 V vs. SCE). Both the results demonstrate that the reversible strain amplitude of the np-Ni samples decreases with increasing frequency, and our np-Ni actuators can give a response even at the high frequency of above 60 mHz.
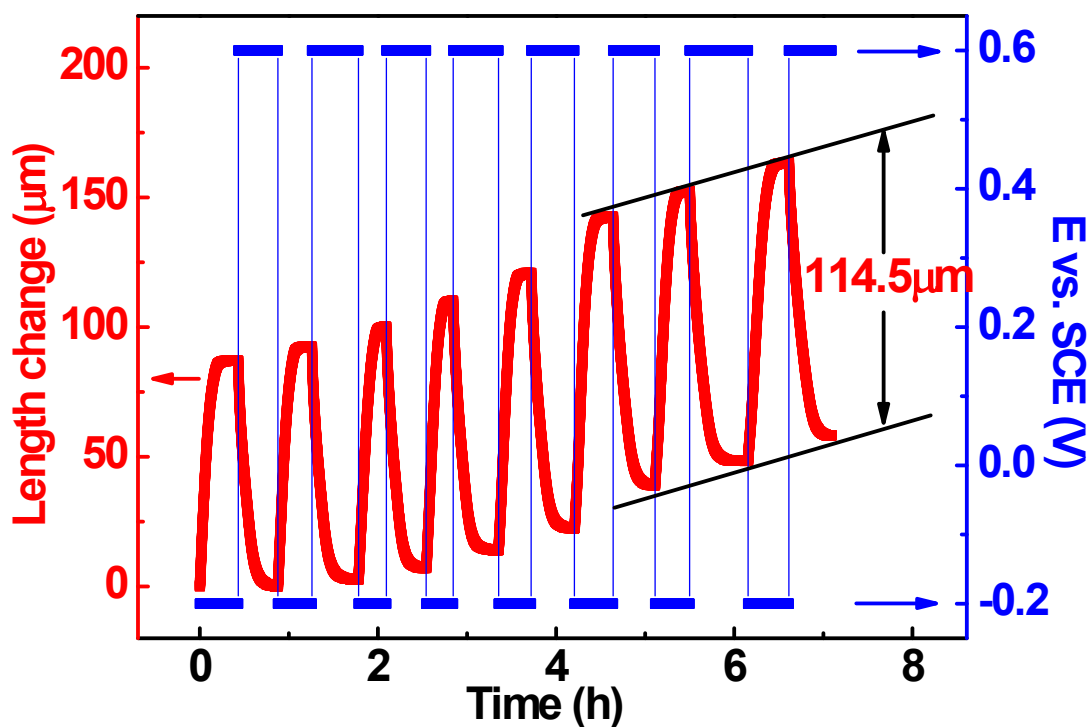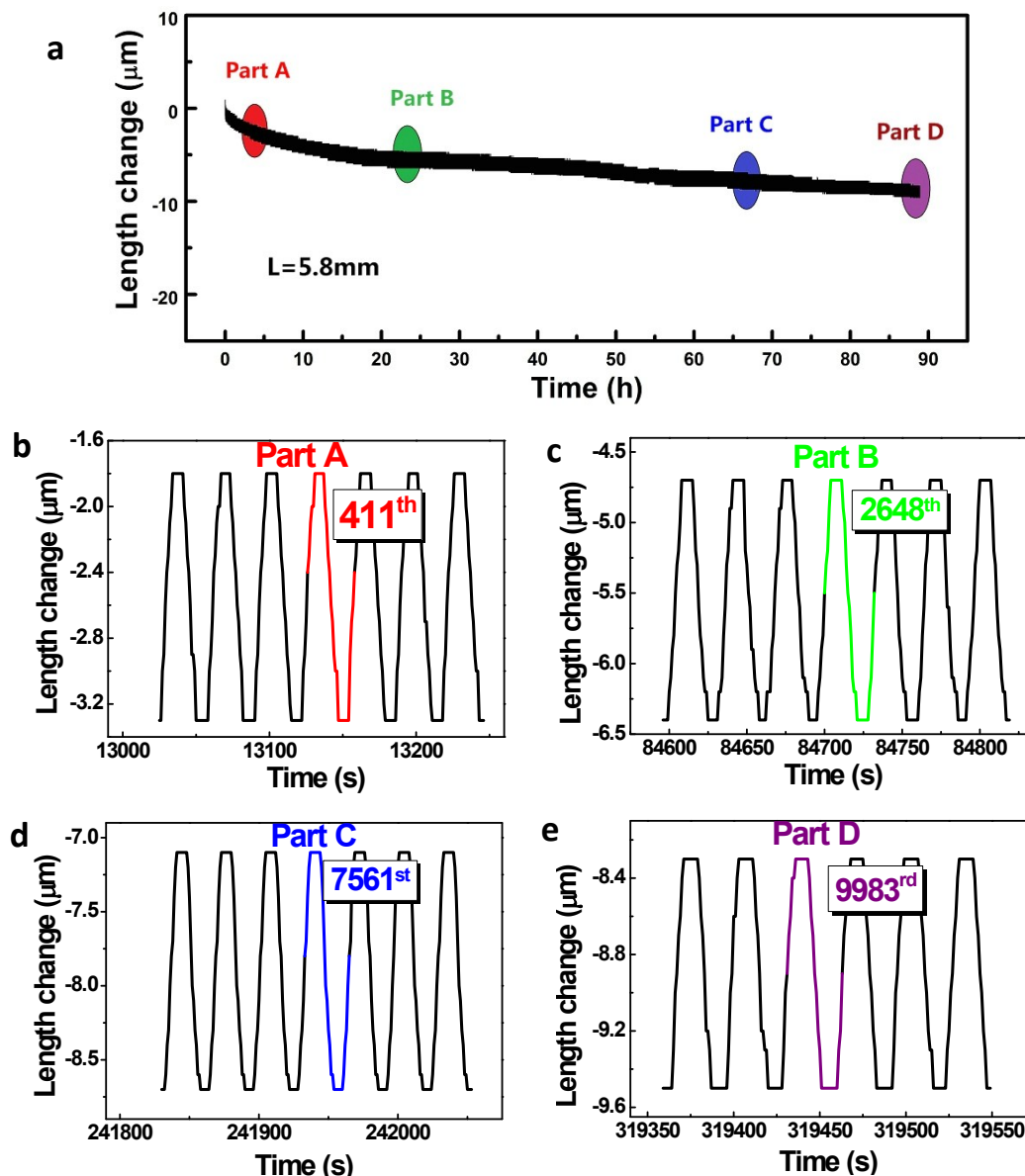
Figure S12 | The reversible length change of the np-Ni sample versus the applied time during the potentiostatic process (the potential was switched from - 0.2 to 0.6V vs. SCE and thus back). The reversible length change of np-Ni could be modulated through switching the potential and changing the applied time at each potential. It is astonishing that the maximum reversible length change could reach up to 114.5 μm for the np-Ni rod with the length of 5.7 mm. This is very important for actuator applications which require large strain strokes.
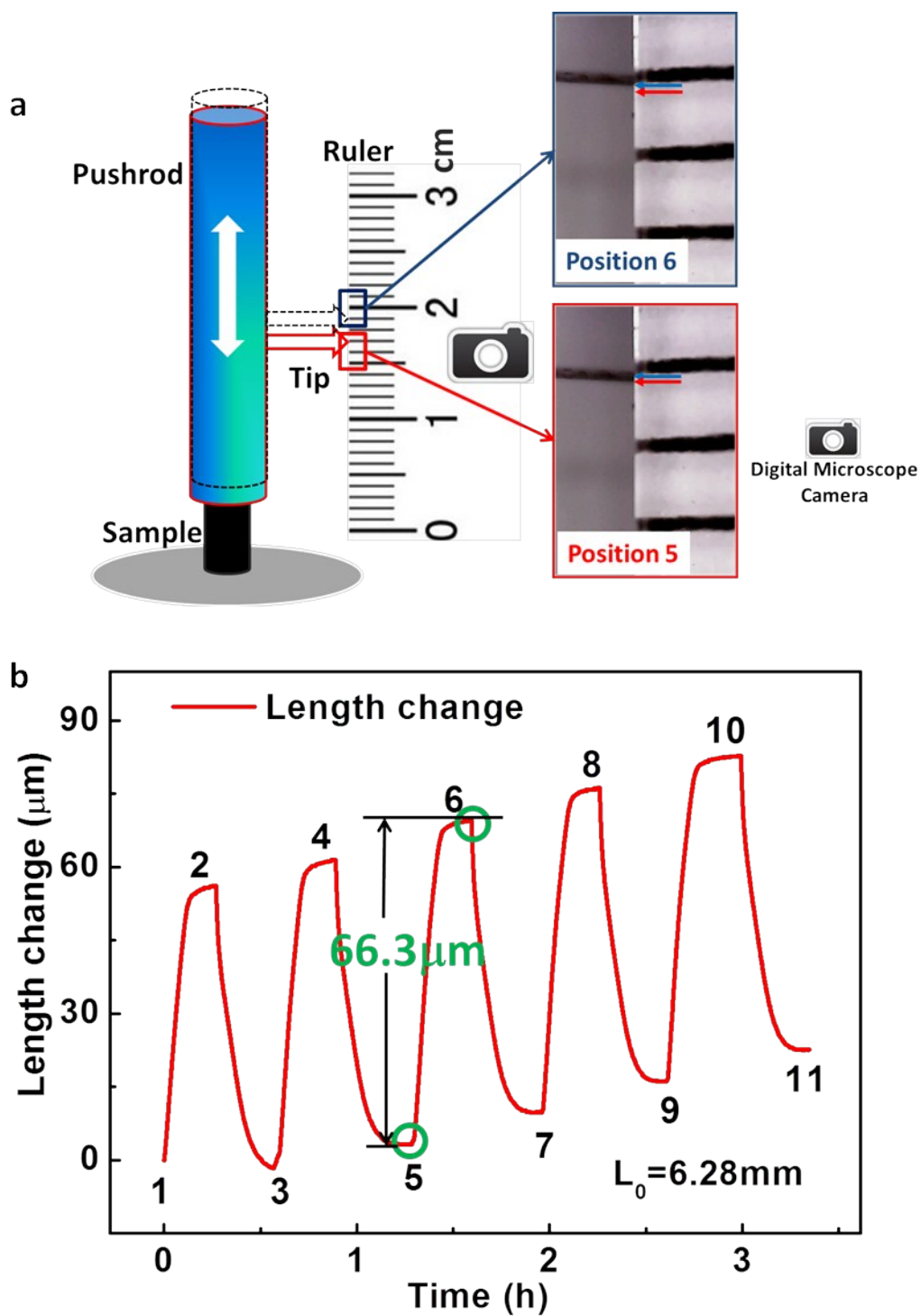
Figure S13 | (**a**) Schematic illustration showing the length change monitored by a digital microscopic camera, when the np-Ni sample was tested by the square wave potential technique (potential window: - 0.2~0.6V vs. SCE). The photographs on the right side show two positions of the pushrod, corresponding to position 5 and 6

denoted by green circles in (b) respectively. At position 5, the pushrod was located at the lower site (marked by the red arrow in the photographs), and then moved to the upper site (marked by the blue arrow in the photographs, position 6) due to the charge-induced expansion of the np-Ni rod. In the following step, the pushrod would move back to the lower site owing to the charge-induced contraction of the np-Ni rod. This reciprocating motion of the pushrod (corresponding to the reversible expansion/contraction of the np-Ni rod) can be more clearly observed in Flash S1. (**b**) Reversible length change of the np-Ni versus time during the square wave potential process (five successive cycles). The present results show that large strain strokes could be obtained in the np-Ni samples due to their bulk sizes and giant strain.

Figure S14 | (a) The reversible length change of the np-Ni sample versus time during 10,000 successive CV processes at the scan rate of 50 mV/s (potential window: -0.2~0.6 V vs. SCE). The initial length of the np-Ni rod is 5.8 mm. Although the irreversible length change could be observed, the superimposed reversible strain with the comparable amplitude indicates the excellent long-term stability of our np-Ni samples. Four selected parts are presented in (b-e) as enlarged views. Part A-D are highlighted in (a) by solid ellipses with different colors. The typical reversible length changes at different times are also highlighted in (b-e) using different colors (**b**: red in

27

Part A, 411th; **c**: green in Part B, 2648th; **d**: blue in Part C, 7561st; **e**: purple in Part D, 9983rd). The long-term stability of our np-Ni samples is quite important for their commercial applications as actuator materials[10].

Table S1 | Stress-charge coefficients (ζ) of the np-Ni samples compared with other nanoporous metals reported in the literature.

Materials	Measurement technique	Electrolyte	Potential range (V)	$\zeta(V)$
np-Au[14]	CV	1M HClO$_4$	0.7 to 1 vs. Ag/AgCl	+2.0
		0.3M NaF	-0.2 to 0.9 vs. Ag/AgCl	+4.7
np-Pt[15]	CV	0.7M NaF	0.1 to 1.0 vs. Ag/AgCl	+1.6
	CV	5M NaOH	-0.2 to 0.6 vs. SCE	+1.5~+2.8
np-Ni	Square wave potential	5M NaOH	-0.05~0.4 vs. SCE	+3.4
(this work)	Square wave potential	5M NaOH	-0.15~0.5 vs. SCE	+3.0
	Square wave potential	5M NaOH	-0.25~0.6 vs. SCE	+2.6

Table S2 | Total transferred charge (ΔQ), surface stress-charge coefficients (ζ) and maximum variations in surface stress (Δf) of the np-Ni sample during the CV processes at different scan rates (potential window: - 0.2~0.6 V vs. SCE).

Scan rate (*mV/s*)	ΔQ (*C*)	ζ (*V*)	Δf (*N/m*)
50	1.0	+2.8	0.6
20	2.3	+2.5	1.2
10	4.5	+2.2	2.1
5	8.1	+1.8	3.2
2	17.2	+1.7	6.7
1	26.3	+1.5	10.0
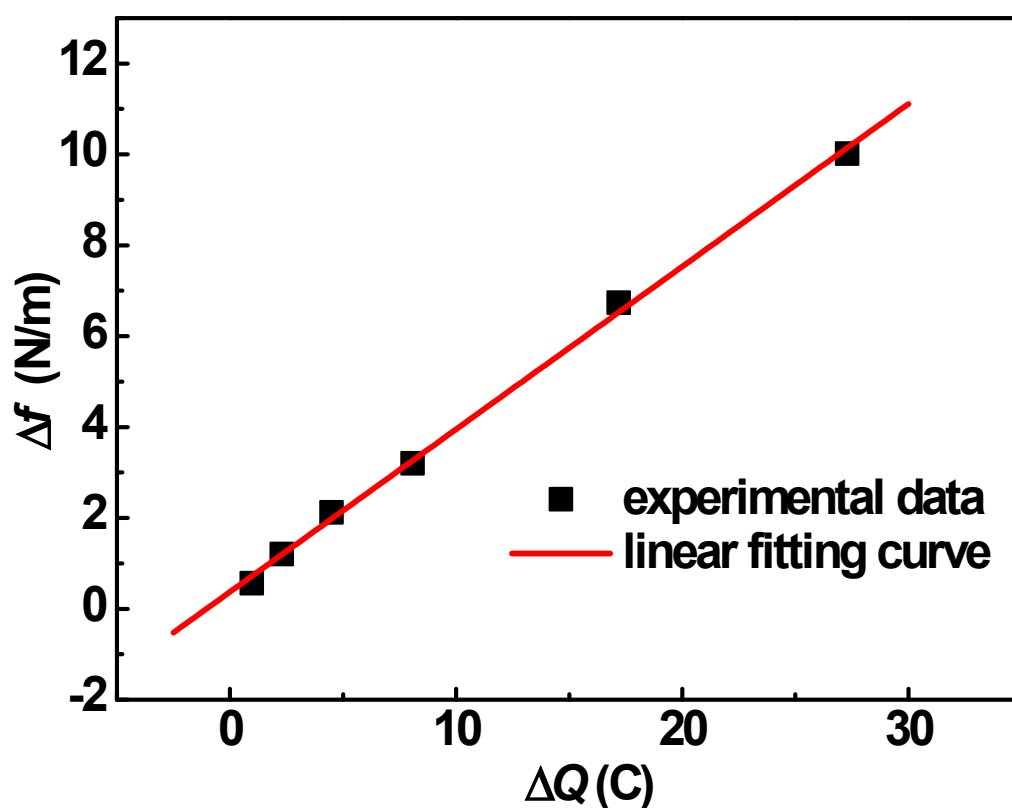
Figure S15 | The maximum variations in surface stress (Δf) of the np-Ni sample versus the total transferred charge (ΔQ) during the CV processes at different scan rates (potential window: - 0.2~0.6 V vs. SCE). An approximate linear correlation could be observed between these two factors. It is obvious that we can maximize the reversible strain amplitude of our np-Ni actuators through increasing the surface transferred charge which is associated with their nanoporous microstructure and specific surface area. The present results provide us a hint to enhance the performance of metallic actuators. Of course, we should also take into consideration the intrinsic strength of nanoporous metallic actuators.

Table S3 | Figures of merit for various nanoporous metallic actuators.[a]

| Materials	Y (MPa)	ε_{max} (10^{-4})	w_V (KJ/m^3)	w_M (J/Kg)	*Stroke* (μm)	*Price*[b] (USD/lb)
np Pt[11,15]	9000	15	90	30	2.5	22503
np Au[14]	25000	24	720[c]	150[c]	4.5	20217
np Ag[20]	6600[c]	50	80[c]	26[c]	4.5	312
np Au-Pt[16] linear-	25000	130	2000	400	26	20442
volumetric-	25000	390	6000	1200	/	/
np Nickel linear-	19600	200	3920	1468	114	7.1
volumetric-	19600	600	11760	4404	/	/

[a] Y: Young's modulus, ε_{max}: maximum strain amplitude, w_V: volume-specific strain energy density,
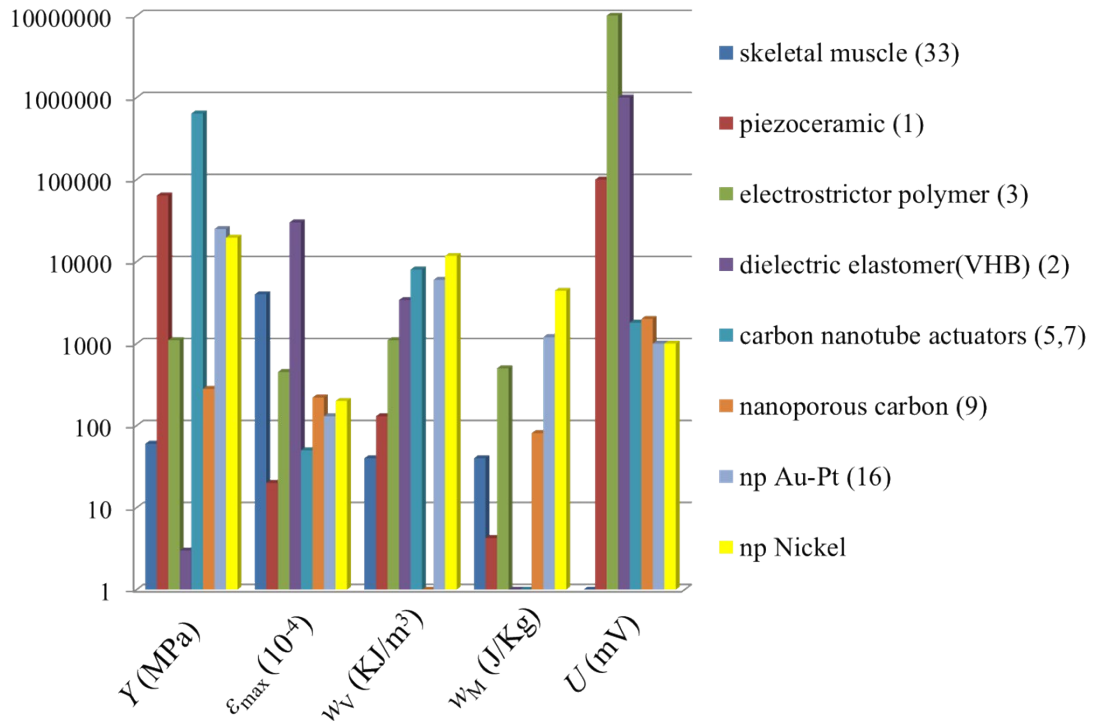
w_M: mass-specific strain energy density.

[b] The data comes from the London Metal Exchange recorded at April 1st, 2014.

[c] These values were calculated from the data provided in the related literature.
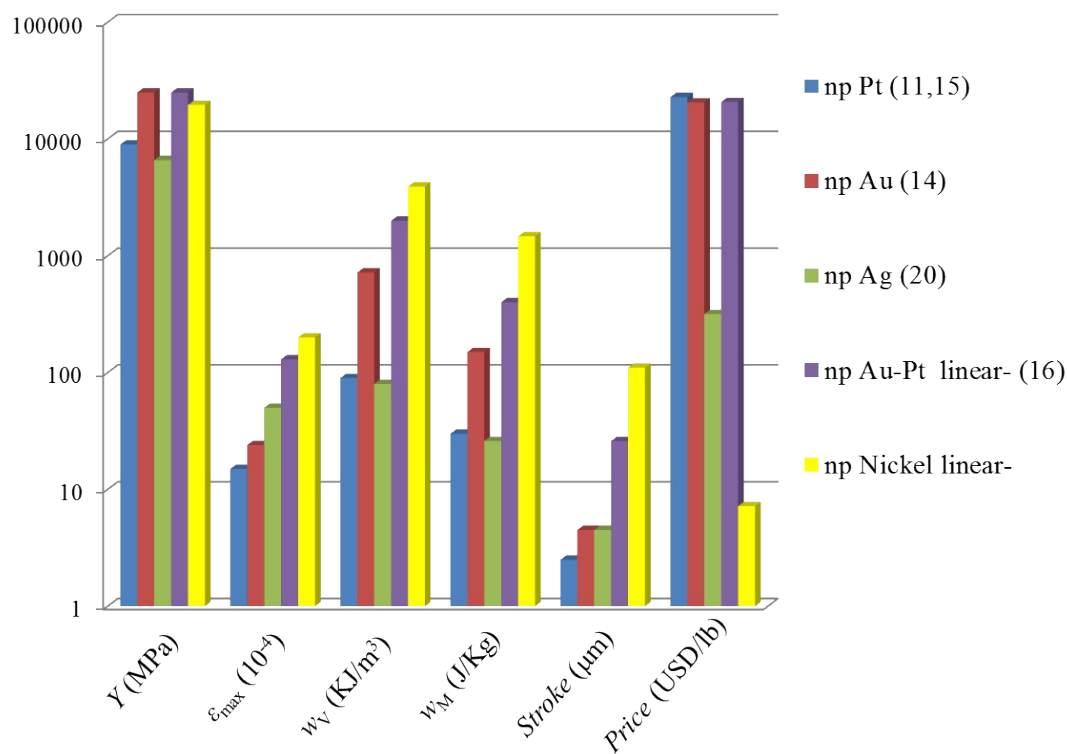
Figure S16 | Column chart plot of characteristics of various nanoporous metallic actuator materials. Y: Young's modulus, ε_{max}: maximum strain amplitude, w_V: volume-specific strain energy density, w_M: mass-specific strain energy density. Clearly, our np-Ni actuators show the best over-all properties (comparable modulus, maximum reversible strain and maximum strain energy density) and the lowest price which are crucial for their commercial applications as metallic actuators or metallic muscles.

Figure S17 | Column chart plot of characteristics of various actuator materials. Y: Young's modulus, ε_{max}: maximum strain amplitude, w_V: volume-specific strain energy density, w_M: mass-specific strain energy density, U: operating voltage for 100 μm actuator size. The data are the same as those in Table 1. The references are also consistent with those listed in Table 1.
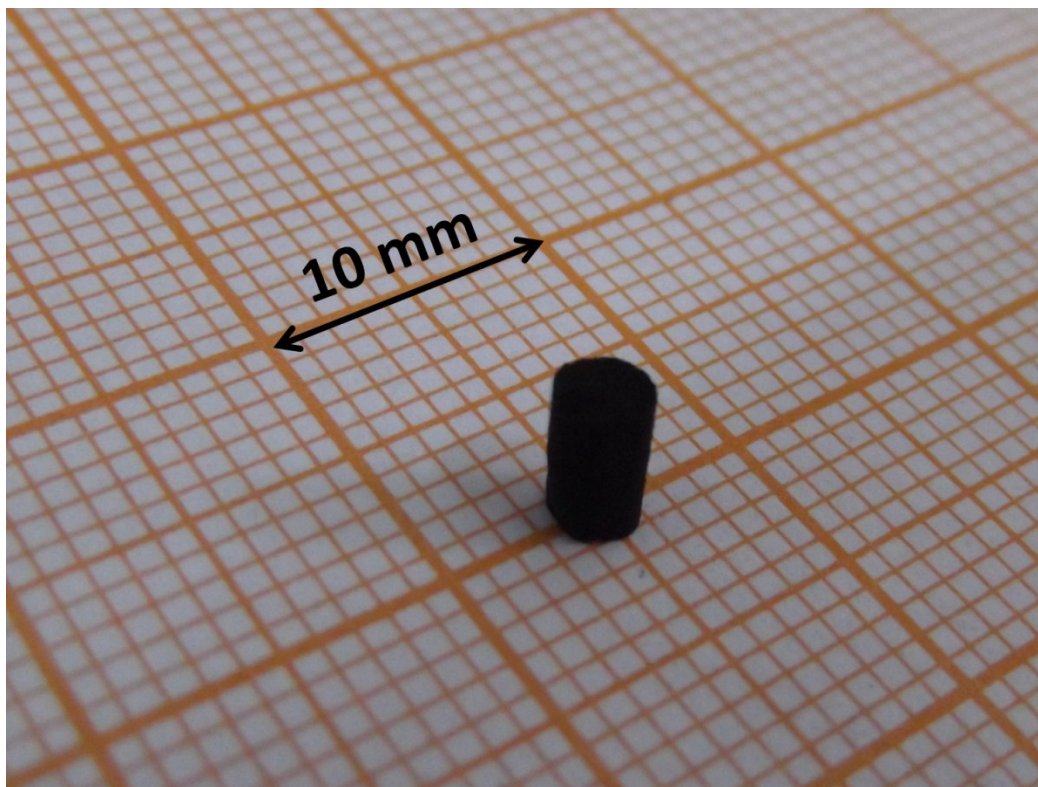
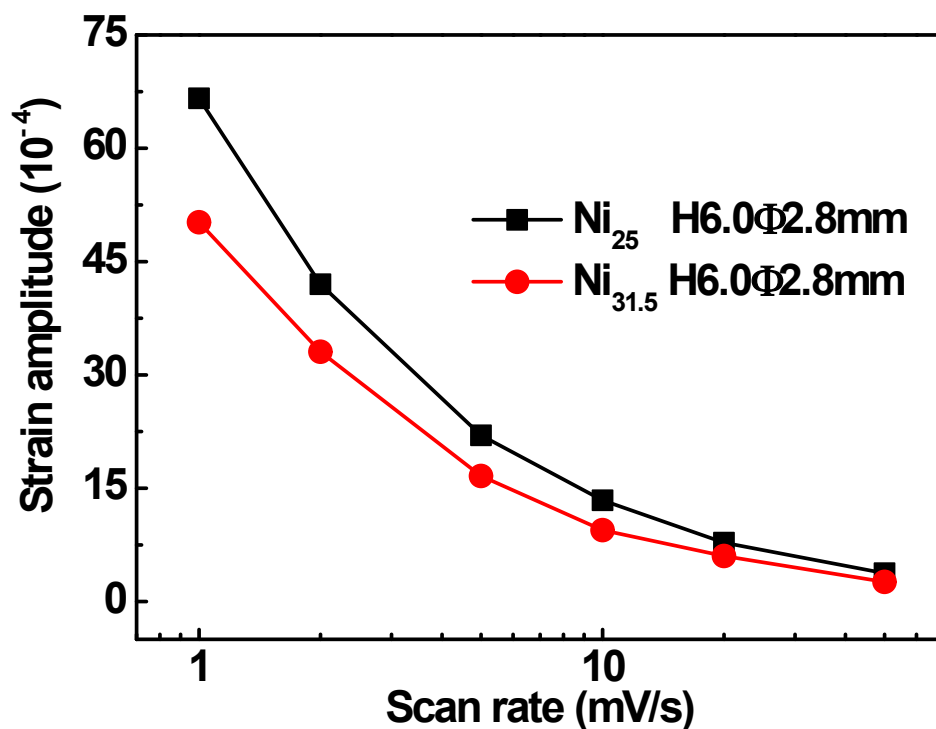**Figure S18** | Macrograph of a nanoporous cobalt (np-Co) rod.

Figure S19 | The reversible strain amplitude of the np-Ni samples versus the scan rate during the CV processes with the potential window of - 0.2~0.6 V vs. SCE. The 'Ni$_{25}$' denotes the np-Ni sample which was prepared by the dealloying of the Al$_{75}$Ni$_{25}$ precursor in the 6 M KOH solution, and the 'Ni$_{31.5}$' denotes the np-Ni sample which was prepared by the dealloying of the Al$_{68.5}$Ni$_{31.5}$ precursor. Both the two np-Ni samples show good electrochemical actuation properties in the 5 M NaOH solution.
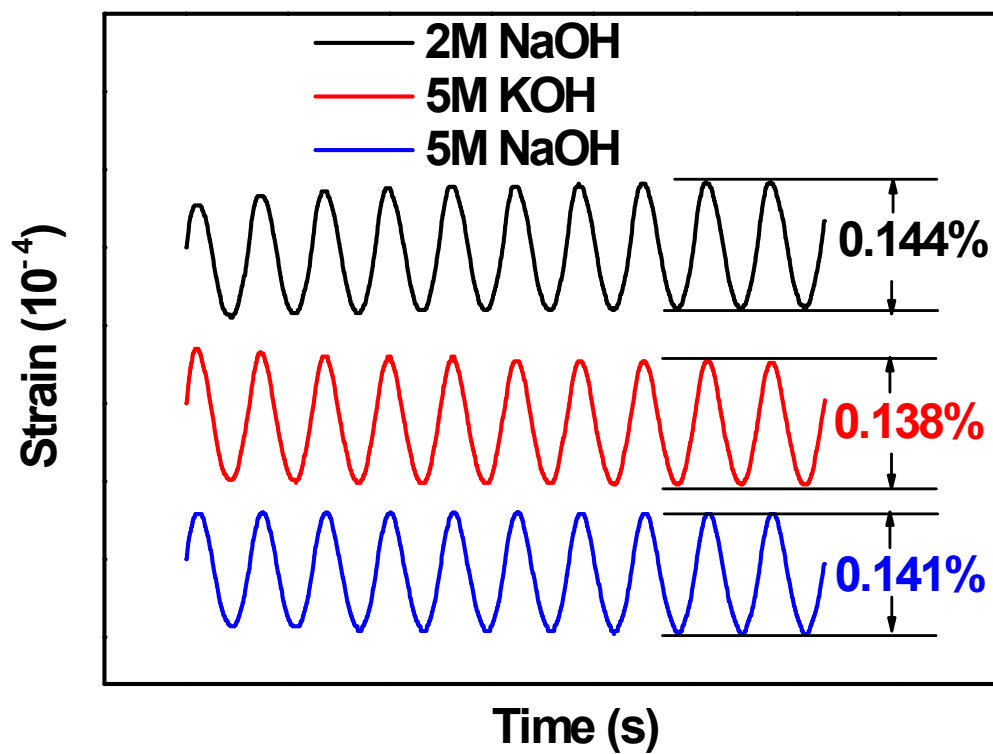
Figure S20 | The reversible strain of the np-Ni sample versus time during the CV processes with the potential window of - 0.2~0.6 V vs. SCE at the scan rate of 10 mV/s. It can be seen that similar electrochemical actuation properties (reversible strain amplitude and stability) could be obtained for the np-Ni sample in different alkaline electrolytes with different concentrations.

7. References

1. Cross, L. E. Ferroelectric materials for electromechanical transducer applications. *Mater. Chem. Phys.* **43,** 108-115 (1996).

2. Pelrine, R., Kornbluh, R., Pei, Q. & Joseph, J. High-Speed Electrically Actuated Elastomers with Strain Greater Than 100%. *Science* **287,** 836-839 (2000).

3. Zhang, Q. M., Bharti, V. & Zhao, X. Giant Electrostriction and Relaxor Ferroelectric Behavior in Electron-Irradiated Poly(vinylidene fluoride-trifluoroethylene) Copolymer. *Science* **280,** 2101-2104 (1998).

4. Baughman, R. H. Conducting polymer artificial muscles. *Synth. Met.* **78,** 339-353 (1996).

5. Baughman, R. H*., et al.* Carbon Nanotube Actuators. *Science* **284,** 1340-1344 (1999).

6. Kohl, M. *Shape Memory Microactuators* (Springer, Berlin, 2004).

7. Hughes, M. & Spinks, G. M. Multiwalled Carbon Nanotube Actuators. *Adv. Mater.* **17,** 443-446 (2005).

8. Xie, X*., et al.* An Asymmetrically Surface-Modified Graphene Film Electrochemical Actuator. *ACS Nano* **4,** 6050-6054 (2010).

9. Shao, L.-H*., et al.* Electrically Tunable Nanoporous Carbon Hybrid Actuators. *Adv. Funct. Mater.* **22,** 3029-3034 (2012).

10. Biener, J*., et al.* Surface-chemistry-driven actuation in nanoporous gold. *Nat. Mater.* **8,** 47-51 (2009).

11. Weissmüller, J*., et al.* Charge-Induced Reversible Strain in a Metal. *Science* **300,** 312-315 (2003).

12. Kramer, D., Viswanath, R. N. & Weissmüller, J. Surface-Stress Induced Macroscopic Bending of Nanoporous Gold Cantilevers. *Nano Lett.* **4,** 793-796 (2004).

13. Kramer, D. & Weissmüller, J. A note on surface stress and surface tension and their interrelation via Shuttleworth's equation and the Lippmann equation. *Surf. Sci.* **601,** 3042-3051 (2007).

14. Jin, H.-J., Parida, S., Kramer, D. & Weissmüller, J. Sign-inverted surface stress-charge response in nanoporous gold. *Surf. Sci.* **602,** 3588-3594 (2008).

15. Viswanath, R. N., Kramer, D. & Weissmüller, J. Adsorbate effects on the surface stress–charge response of platinum electrodes. *Electrochim. Acta* **53,** 2757-2767 (2008).

16. Jin, H.-J.*, et al.* Nanoporous Au−Pt Alloys As Large Strain Electrochemical Actuators. *Nano Lett.* **10,** 187-194 (2010).

17. Detsi, E., Punzhin, S., Rao, J., Onck, P. R. & De Hosson, J. T. M. Enhanced Strain in Functional Nanoporous Gold with a Dual Microscopic Length Scale Structure. *ACS Nano* **6,** 3734-3744 (2012).

18. Detsi, E., Onck, P. & De Hosson, J. T. M. Metallic Muscles at Work: High Rate Actuation in Nanoporous Gold/Polyaniline Composites. *ACS Nano* **7,** 4299-4306 (2013).

19. Viswanath, R. N. & Weissmüller, J. Electrocapillary coupling coefficients for hydrogen electrosorption on palladium. *Acta Mater.* **61,** 6301-6309 (2013).

20. Detsi, E., Sellès, M. S., Onck, P. R. & De Hosson, J. T. M. Nanoporous silver as electrochemical actuator. *Scripta Mater.* **69,** 195-198 (2013).

21. Cheng, C. & Ngan, AHW. Reversible Electrochemical Actuation of Metallic Nanohoneycombs Induced by Pseudocapacitive Redox Processes. *ACS Nano* **9,** 3984-3995 (2015).

22. Haiss, W. Surface stress of clean and adsorbate-covered solids. *Rep. Prog. Phys.* **64,** 591-648 (2001).

23. Weissmüller, J. & Cahn, J. W. Mean stresses in microstructures due to interface stresses: A generalization of a capillary equation for solids. *Acta Mater.* **45,** 1899-1906 (1997).

24. Baughman, R. H. Muscles Made from Metal. *Science* **300,** 268-269 (2003).

25. Erlebacher, J., Aziz, M. J., Karma, A., Dimitrov, N. & Sieradzki, K. Evolution of nanoporosity in dealloying. *Nature* **410,** 450-453 (2001).

26. Erlebacher, J. An Atomistic Description of Dealloying: Porosity Evolution, the Critical Potential, and Rate-Limiting Behavior. *J. Electrochem. Soc.* **151,** C614-C626 (2004).

27. Crowson, D. A., Farkas, D. & Corcoran, S. G. Mechanical stability of nanoporous metals with small ligament sizes. *Scripta Mater.* **61,** 497-499 (2009).

28. Hakamada, M., Matsumura, S. & Mabuchi, M. Electrochemical actuation of nanoporous Ni in NaOH solution. *Mater. Lett.* **70,** 132-134 (2012).

29. Liu, K. C. & Anderson, M. A. Porous Nickel Oxide/Nickel Films for Electrochemical Capacitors. *J. Electrochem. Soc.* **143,** 124-130 (1996).

30. Weissmüller, J., Newman, R. C., Jin, H.-J., Hodge, A. M. & Kysar, J. W. Nanoporous metals by alloy corrosion: formation and mechanical properties. *MRS Bull.* **34,** 577-

586 (2009).

31.   Biener, J., Hodge, A. M., Hamza, A. V., Hsiung, L. M. & Satcher, J. H. Nanoporous Au: A high yield strength material. *J. Appl. Phys.* **97,** 024301 (2005).

32.   Ledbetter, H. M. & Reed, R. P. Elastic Properties of Metals and Alloys, I. Iron, Nickel, and IronNickel Alloys. *J. Phys. Chem. Ref. Data* **2,** 531-618 (1973).

33.   Madden, J. D. W., *et al.* Artificial muscle technology: physical principles and naval prospects. *IEEE J. Oceanic Eng.* **29,** 706-728 (2004).

34.   Parida, S., *et al.* Volume Change during the Formation of Nanoporous Gold by Dealloying. *Phys. Rev. Lett.* **97,** 035504 (2006).

35.   Qi, Z., *et al.* Alloy composition dependence of formation of porous Ni prepared by rapid solidification and chemical dealloying. *J. Alloys Compd.* **472,** 71-78 (2009).

36.   Li, H. B., *et al.* Amorphous nickel hydroxide nanospheres with ultrahigh capacitance and energy density as electrochemical pseudocapacitor materials. *Nat. Commun.* **4,** 1894 (2013).

37.   Sieradzki, K., Corderman, R. R., Shukla, K. Computer simulations of corrosion: Selective dissolution of binary alloys. *Philos. Mag. A* **59**, 713 (1989).

38.   Wang, Y., Xu, J. & Wu, B. Chloride ion effect and alloying effect on dealloying-induced formation of nanoporous AuPt alloy. *Appl. Surf. Sci.* **276,** 262-268 (2013).